Magnetocaloric effect near room temperature in a freestanding two-dimensional non–van der Waals crystal of MnCoAs

Qinxi Liu,[1,2] Ying Liu,[2] Xue Jiang,[1,2,*] Yan Qi,[3,†] Junfeng Gao,[1,2] and Jijun Zhao[1,2]

[1]*State Key Laboratory of Structural Analysis for Industrial Equipment, Dalian University of Technology, Dalian 116024, China*
[2]*Key Laboratory of Material Modification by Laser, Ion and Electron Beams (Dalian University of Technology), Ministry of Education, Dalian 116024, China*
[3]*School of Physics and Materials Engineering, Dalian Minzu University, Dalian 116600, China*

(Received 4 December 2022; revised 2 June 2023; accepted 3 August 2023; published 18 August 2023)

The magnetocaloric effect (MCE) plays a major role in magnetic refrigeration. However, a large MCE near room temperature has rarely been observed in the fast-growing family of two-dimensional (2D) materials. Using 2D non–van der Waals crystals, herein we design an intrinsic and physically realistic system to achieve a large MCE. Based on first-principles calculations, we identify that 2D MnCoAs is a robust ferromagnetic metal, whose specific heat shows anomalous bimodal behavior. The MCE in 2D MnCoAs generates a Curie temperature of 214–221 K, a magnetic entropy change of $1.4-4.3\,\mathrm{J\,kg^{-1}\,K^{-1}}$, a relative cooling power of $28.4-244.5\,\mathrm{J\,kg^{-1}}$, and a full width at half maximum of the entropy change peak of 20–57 K for a magnetic field change of 1–7 T. For comparison, the value of magnetic entropy change is $0-0.2\,\mathrm{J\,kg^{-1}\,K^{-1}}$ in bulk MnCoAs. Obviously, the reduced dimensionality leads to a significant improvement in the MCE. In addition, 2D MnCoAs is highly ductile, which is conducive to magnetic refrigeration cycling stability. We also show that a 2D MnCoAs crystal can be grown on a Si (001) substrate while it retains its MCE value, paving an avenue to the desired goal of on-chip cooling. Our results provide not only an alternative MCE thin film for cooling applications in nanodevices, but also a fundamental understanding of the impact of reduced dimensionality on MCE.

DOI: 10.1103/PhysRevB.108.054427

I. INTRODUCTION

The magnetocaloric effect (MCE) is defined as the temperature change of a magnetic material upon applying an external magnetic field. There has been great interest in utilizing this effect for magnetic refrigeration, which provides the prospect of an environmentally friendly and cost-effective cooling technology alternative to conventional vapor compressor refrigeration [1,2].The rapid development of two-dimensional (2D) magnetic materials over the past decade has opened an avenue for their potential use in nanoscale cooling, lab-on-chip cooling, thermal switches, and microrefrigerators [3,4], satisfying the trend for miniaturization of devices.

Most three-dimensional (3D) magnetocaloric materials with large MCE have a first-order magnetostructural transition, resulting from their strong spin-lattice interaction [5]. For the 2D systems, the effect of the reduced dimensionality on the magnetic and magnetocaloric response of materials remains unclear. Recently, the MCE on magnetic films including FeRh, Fe_2Ta, $EuTiO_3$, $Gd_{100-x}Co_x$ and Mn-Ni-*X* systems has been reported [6–11]. In general, the decrease in dimensionality of magnetic materials leads to a decrease in Curie temperature (T_C), saturation magnetization, and the magnitude of magnetic entropy change [8,12]. For example, Hung *et al.* reported that MnP film have a low MCE of $0.6\,\mathrm{J\,kg^{-1}\,K^{-1}}$ compared to bulk compounds [13]. Moreover, the quality of the films also affects the evaluation of their magnetocaloric properties. Lampen-Kelley *et al.* showed that the MCE in $EuO_{1-\delta}$ thin films is sensitive to the oxygen vacancies [14]. Compared with the MCE of intrinsic magnetocaloric materials, the proximity-induced MCE is generally not robust [15]. Simultaneously, the experimentally measured critical temperatures of 2D magnetocaloric films such as $Gd_5Si_{1.3}Ge_{2.7}$ [16], $[(CH_2)_2(NH_3)_2]CuCl_4$ [17], $(C_{12}H_{25}NH_3)_2CuCl_4$ [18], and oxalate-bridged Gd-based MOF [19] are 194, 34, 13, and 2 K, respectively. Such low magnetic transition temperatures significantly hinder the application of magnetic devices at room temperature.

Compared to 2D van der Waals (vdW) compounds, 2D non-vdW materials are derived from a nonlayered bulk counterpart with strong chemical bonds in all three dimensions, rather than weak interlayer vdW interaction [20]. Recent experiments have made a significant breakthrough in the synthesis of high-quality 2D non-vdW magnetic materials. This emerging family of 2D materials has many advantages in the context of designing magnetocaloric materials with large MCE. Using advanced synthesis techniques, such as chemical vapor deposition (CVD) and molecular beam epitaxy (MBE), a number of high-quality 2D non-vdW magnetic materials have been recently obtained, including 2D Cr_mX_n (X = Te and Se) [21–26], FeX [27,28], and α-$MnSe_2$ [29] ultrathin films. These systems exhibit robust ferromagnetism with a high Curie temperature (T_C) of 125–367 K. In addition, 2D non-vdW materials exhibit good electronic and thermal

*Corresponding author: jiangx@dlut.edu.cn
†Corresponding author: qiyan@dlnu.edu.cn

conductivity and high mechanical strength [30–32], suggesting their great potential as magnetocaloric materials with high thermal cycling stability. In addition, the surfaces of 2D non-vdW materials possess abundant dangling bonds. Hence, their MCE may be improved by structural modifications, such as decoration with metal atoms, surface passivation, and forming heterostructures [20]. All these suggest that a large MCE could emerge in 2D non-vdW compounds.

In this paper, we predict the 2D non-vdW ferromagnetic metal MnCoAs from first-principles calculations. It has good thermal stability, excellent ductility, and an appreciable Curie temperature up to 221 K. The coexistence of a large magnetic moment (3.3 μ_B/Mn) and a weak out-of-plane magnetic anisotropy energy (0.17 meV/formula) allows easy control of the polarization of MnCoAs ultrathin film under an external magnetic field, while Mn-Co interaction could act as an additional internal field to further polarize the Mn ions when an external field is applied. These two polarization mechanisms cause abnormal bimodal behavior in the specific heat of 2D MnCoAs. Therefore, 2D MnCoAs has a large magnetic entropy change, a high relative cooling power (RCP), and a wide operating temperature range. Moreover, 2D MnCoAs crystal might be grown on a Si (001) substrate and retains its magnetic properties. To clarify the dimensional effect, the critical MCE parameters of bulk MnCoAs are also calculated for comparison. A similar magnetocaloric response and even larger MCE ($\Delta S_m = 4.7\,\mathrm{J\,kg^{-1}\,K^{-1}}$) were observed in 2D MnNiAs.

II. COMPUTATIONAL METHODS

Our calculations were performed using spin-polarized density functional theory (DFT) with plane-wave basis sets (cutoff energy of 600 eV), as implemented in the Vienna *ab initio* simulation package (VASP) [33,34]. Projector augmented wave (PAW) potentials were used to describe the ion-electron interactions [35]. Exchange-correlation interactions were described using the Perdew-Burke-Ernzerhof (PBE) functional within generalized gradient approximation [36]. A vacuum space of 15 Å thickness was added to avoid interactions between repeated images with periodic boundary condition. The reciprocal space was sampled with 0.02 $\mathrm{Å^{-1}}$ spacing in a Monkhorst-Pack scheme for structural optimization. Both the lattice constants and atomic positions were fully relaxed until the force was less than $10^{-2}\,\mathrm{eV/Å^{-1}}$ and the change in total energy was less than 10^{-6} eV, respectively. Phonon dispersion calculations were carried out using the finite displacement method implemented in the PHONOPY program [37]. To confirm the thermal stability of the MnCoAs compound, *ab initio* molecular dynamics (AIMD) simulation within the *NVT* canonical ensemble was performed [38]. During the AIMD simulation, a $5 \times 5 \times 1$ supercell was kept at 300 K, and the simulation lasted for 5 ps with a time step of 1 fs.

Regarding nearest-neighbor magnetic-exchange interactions, the Hamiltonian of a classical Heisenberg model can be written as

$$\eta = -\sum_{i,j} J_1 M_i M_j - \sum_{k,l} J_2 M_k M_l - \sum_{m,n} J_3 M_m M_n, \quad (1)$$

where J_1, J_2, and J_3 are the first, second, and third nearest-neighbor exchange parameters, respectively, and M is the on-site spin magnetic moment. Meanwhile, magnetic anisotropy energy (MAE) is defined as [39]

$$\mathrm{MAE} = E_{\mathrm{tot}}[\parallel] - E_{\mathrm{tot}}[\perp], \quad (2)$$

where $E_{\mathrm{tot}}[\parallel]$ and $E_{\mathrm{tot}}[\perp]$ are the total energies of states, with magnetization directions parallel and perpendicular to the horizontal plane, respectively. Monte Carlo (MC) simulation is an effective approach for computing the magnetothermal properties of a system at finite temperatures. Here we used a Potts-like Ising model to perform the MC simulation [40] (see Supplemental Material Scheme 1 for more details [41]; also see [42–46] therein).

III. RESULTS AND DISCUSSION

Inspired by the experimentally demonstrated Mn-based magnetocaloric materials [13,47–50], we explore the possible MCE in a 2D non-vdW crystal of MnCoAs. Supplemental Material Fig. S1 [41] depicts the atomic structures and equation of state of several possible phases of the MnCoAs crystal, including orthorhombic (no. 62) [51], hexagonal (no. 189), cubic (no. 216), and tetragonal (no. 129) ones, some of which are taken from MnNiAs and MnFeAs solids. Among them, our DFT calculations show that the tetragonal phase is energetically most stable under ambient conditions, and the calculated phonon dispersion indicates its dynamic stability. Inheriting from its 3D counterparts, 2D MnCoAs down to single unit cell thickness crystallizes in a tetragonal lattice with *P*4/*nmm* space group and lattice constant of $a = 3.58$ Å [Fig. 1(a)]. It has a multilayer configuration comprising a Co atomic layer sandwiched between bottom and top MnAs layers. Specifically, each Mn/Co atom is surrounded by four As atoms, forming a tetrahedral $CoAs_4$ unit and square planar $MnAs_4$ unit, respectively.

To assess the thermodynamic stability of 2D MnCoAs, we compute its formation energy, $E_f = E_{\mathrm{MnCoAs}} - E_{\mathrm{Mn}} - E_{\mathrm{Co}} - E_{\mathrm{As}}$, where E_{Mn}, E_{Co}, and E_{As} are the energy per atom of Mn, Co, and As in their most stable elemental phase, respectively. The formation energy of 2D MnCoAs is calculated to be −0.02 eV/atom, meaning that the chemical synthesis reaction should be exothermic. In Supplemental Material Fig. S2 [41], the calculated phonon dispersion shows an absence of soft phonon modes. As displayed in Supplemental Material Fig. S3 [41], after 5 ps AIMD simulation at 300 K, the 2D MnCoAs supercell retains its geometric structure well. In addition, three nonzero 2D elastic constants (C_{11}, C_{22}, and C_{66}) satisfy the Born-Huang criteria [52]. (Supplemental Material Table S1 [41]) All these results confirm the thermal, thermodynamic, dynamic, and mechanical stability of 2D non-vdW MnCoAs.

Figure 1(b) presents electronic band structure of 2D MnCoAs, showing evident metallic characteristics. According to the atom-projected density of states in Fig. 1(c), such metallicity arises from both Co and Mn atoms. Figures 1(d) and 1(e) show the projected density of states (PDOS) for Co 3*d* and Mn 3*d* orbitals. Clearly, the electronic state at the Fermi level is dominated by both the d_{xz}/d_{yz} orbital of the Co atom and the

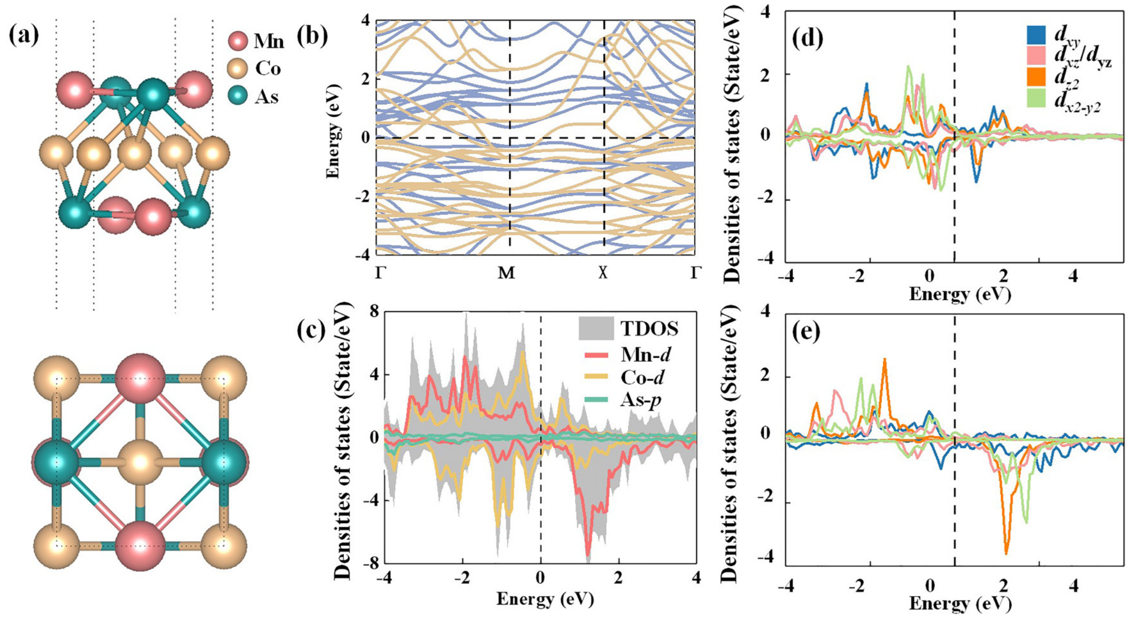

FIG. 1. (a) Side and top views of 2D MnCoAs. The pink, gold, and green spheres correspond to Mn, Co, and As atoms, respectively. (b) Electronic band structure. Orange and blue lines represent the spin-up and spin-down bands, respectively. (c) Total and orbital-projected densities of states for Mn, Co, and As atoms, respectively. The d orbital resolved density of states for (d) Co and (e) Mn atoms in 2D MnCoAs. The Fermi level (black dashed line) is set to zero.

d_{x2-y2} orbital of the Mn atom. The electronic behavior in 2D MnCoAs is further revealed by the charge density and electron localization function (ELF) in Supplemental Material Fig. S4 [41], showing that the electrons are localized around the Mn and Co atoms. Compared to the Co atom, the electrons on the Mn atom are more localized. The calculated Bader charge indicates a net charge transfer of about 0.6 electrons from each Mn atom to its surrounding As atoms. In other words, both localized and itinerant electrons are present in the 2D MnCoAs compound.

To determine the most favorable magnetic ordering, ferromagnetic (FM), ferrimagnetic (FiM), and various antiferromagnetic (AFM) configurations for 2D MnCoAs have been examined in Supplemental Material Fig. S5 [41]. The calculated energy differences among different magnetic configurations are summarized in Supplemental Material Table S2 [41], suggesting the FM ground state for 2D MnCoAs. As presented in Supplemental Material Fig. S6 [41], which shows the spin density distribution of 2D MnCoAs in FM configuration, the magnetism originates mainly from both Mn and Co atoms. As discussed above, each Mn atom sits inside a square planar crystal field formed by four neighboring As atoms. Under D_{4h} symmetry, the crystal field splits the Mn 3d orbitals into four states: d_{xz}/d_{yz}, d_{xy}, d_{x2-y2}, and d_{z2} orbitals. However, the Co atom resides in a distorted tetrahedral coordination because of its T_d symmetry breaking by neighboring Mn atoms. In the tetrahedral crystal field, five degenerate d orbitals of the Co atom should be split into a_1 states (d_{z2} and d_{x2-y2}) and a_2 states (d_{xy}, d_{xz}, and d_{yz}). Distortion of the tetrahedral $CoAs_4$ unit leads to further splitting of the a_1 and a_2 levels; consequently, the d_{xy}, d_{z2}, and d_{x2-y2} orbitals are no longer degenerate. As shown in Fig. 2, the d_{x2-y2} and d_{xz}/d_{yz} orbitals of the Co atom are fully occupied in both spin-up and spin-down channels, while d_{z2} and d_{xy} orbitals are roughly half occupied, resulting in a magnetic moment of 0.2 μ_B for the Co atom. Five d orbitals of the Mn atom in the spin-up channel are fully occupied, while the d_{xy} and d_{xz}/d_{yz} orbitals in the spin-down one are partially filled, giving rise to a magnetic moment of 3.3 μ_B for the Mn atom. This picture is also supported by the occupation numbers of Mn d and Co d orbitals (Supplemental Material Table S3 [41]). In addition, magnetic anisotropy energy (MAE) is an important parameter of a 2D ferromagnet, which preserves long-range FM ordering. From our noncollinear calculations with inclusion of the spin-orbital coupling (SOC) effect, the MAE value in 2D MnCoAs is 0.17 meV per formula, favoring perpendicular anisotropy.

Based on the above discussion about electronic behavior, we inferred that the FM ground state of 2D MnCoAs originates from the coexistence of itinerant and localized magnetism. On one hand, the itinerant electrons in the d_{xy} orbital of Co atoms favor intralayer Co-Co FM coupling. On the other hand, for localized exchange coupling, there is competition between direct- and indirect-exchange coupling. The direct-exchange interaction arising from the overlap of electronic orbitals of the Mn-Co pair is short range. Meanwhile, long-range indirect-exchange coupling is rationalized by Ruderman-Kittel-Kasuya-Yosida (RKKY) and superexchange mechanisms. The on-site magnetic moments interact effectively through an indirect-exchange process mediated by either As atoms or conduction electrons [46,53]. Previously, the above magnetic coupling mechanisms have also been found in tetragonal solids of Fe_2As and MnFeAs [54,55]. In 2D MnCoAs, Mn-Co and Co-Co coupling prefer FM coupling, while indirect Mn(Co)-As-Mn(Co) and Mn-Co-Mn exchange interaction favor AFM coupling. The detailed magnetic-exchange

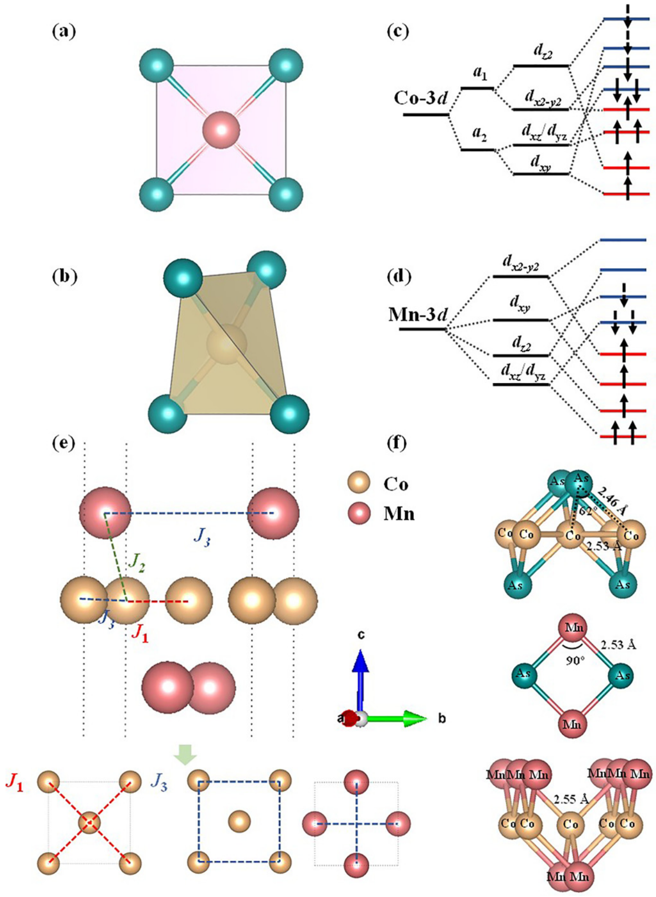

FIG. 2. Schematic structure of (a) square planar and (b) tetrahedral coordination in 2D MnCoAs compound. Schematic representation of d orbital splitting of (c) Co and (d) Mn atoms. (e) Side view showing magnetic-exchange parameters J_1, J_2, and J_3 in a 2D MnCoAs crystal. (f) Schematic representation of the exchange parameters J_3, together with the magnetic paths for these parameters in 2D MnCoAs.

paths and evolution of magnetic interactions in 2D MnCoAs are discussed in Supplemental Material Scheme 2 and Figs. S7 and S8 [41].

In 2D MnCoAs, there are three types of exchange interactions between magnetic ions, corresponding to first, second, and third nearest neighbor exchange constants J_1, J_2, and J_3, as shown in Fig. 2(e). A positive J favors FM ordering, while a negative J favors AFM ordering. For nearest-neighbor intralayer Co-Co exchange (2.53 Å), the itinerant magnetism yields a value of 23.4 meV for J_1. Another shortest interaction, the second nearest neighbor Mn-Co interlayer exchange with interatomic distance of 2.55 Å, involves significant orbital overlap and may be identified as the direct-exchange pathway. Therefore, the calculated J_2 value is 8.1 meV, giving rise to FM coupling. However, the shorter Co-As and Mn-As bonds mean that long-range magnetic coupling in the third nearest neighbor Mn(Co)-Mn(Co) exchange (3.58 Å) is mediated by Mn(Co)-As-Mn(Co) superexchange coupling. Moreover, the third-nearest Mn-Mn exchange interaction also occurs across the square of the Co atoms, which is a combination of RKKY and superexchange interaction. The competition between 90° Mn(Co)-As-Mn(Co) AFM superexchange and Mn-Co-Mn RKKY interaction leads to a J_3 value of −0.9 meV.

As an intrinsic feature of magnetic materials, the MCE of 2D MnCoAs has been further examined. Compared with other 2D magnets, the following features make 2D MnCoAs especially attractive as magnetocaloric material. The relatively large magnetic moment of the Mn ion (3.3 μ_B) means that it can be easily polarized by a moderate external magnetic field. Simultaneously, a weak magnetic anisotropy (0.17 meV/formula) allows rapid switching between ordered and disordered magnetization states under an external field, which is essential to induce large magnetic entropy change. As shown in Fig. 3(a), when an external field (Δh) is applied, the total magnetization (M_{total}) increases gradually with decreasing temperature, rather than saturating quickly below T_C. This phenomenon is distinctly different from that in typical ferromagnets [56]. In Figs. 3(b) and 3(c), one can see that the magnetization of the Co sublattice indeed behaves like a typical ferromagnet that has full magnetization under T_C, but the magnetization of the Mn sublattice occurs obviously more slowly than the Co sublattice. Compared with the magnetic response curve of the entire 2D MnCoAs, the change of total magnetization with magnetic field is mainly determined by the Mn sublattice. The slow polarization of Mn ions leaves room for a slight increase in the magnetic moment under an external field at low temperatures below T_C. Therefore, a large magnetic entropy change is expected (Fig. 3). Our MC simulation confirms that 2D MnCoAs yields a high T_C of 214 K. Because of the strong intralayer ferromagnetic Co-Co interaction (J_1), the Co sublattice is almost saturated around T_C. Meanwhile, the Mn-Co ferromagnetic interaction (J_2) makes the fully polarized Co sublattice more resistant to thermal fluctuation. These two factors together lead to the high T_C value of 214 K. Furthermore, the T_C value monotonically increases with the external field up to 221 K ($\Delta h = 7$ T).

Figures 3(d)–3(f) display the magnetic specific heat ΔS_m and RCP of 2D MnCoAs. Interestingly, the specific heat exhibits abnormal bimodal behavior; that is, the magnetic specific heat does not drop sharply below T_C, but has a shoulder at low temperatures (T_p). Such bimodal behavior is insensitive to the external field. Due to the unique bimodal behavior, 2D MnCoAs has a wide operating temperature range from 20 K ($\Delta h = 1$ T) to 57 K ($\Delta h = 7$ T). In general, the magnetocaloric films exhibit a wide ΔS_m temperature distribution, resulting in a large RCP value, but the ΔS_m value could decrease significantly. However, 2D MnCoAs retains its huge MCE over a broad operating temperature range, corresponding to the peak width at half height δT_{FWHM} [57] in Figs. 3(e) and 3(f) (from 20 K under 1 T magnetic field to 57 K under 7 T), compared to that of $Gd_5Si_{1.3}Ge_{2.7}$ films (24 K) [16]. The obtained ΔS_m and RCP values are 1.4 J kg^{-1} K and 28.4 J kg^{-1} under a magnetic field of 1 T and 4.3 J kg^{-1} K and 244.5 J kg^{-1} under 7 T, respectively. Notably, the ΔS_m value for 2D MnCoAs is much higher than the values recently reported for 3D layered magnetocaloric materials such as $Fe_{3-x}GeTe_2$ (1.2 J kg^{-1} K^{-1}) [58] and VI_3 (0.95 J kg^{-1} K^{-1}) [59]. In magnetocaloric films (Table I), the ΔS_m value of 2D MnCoAs is slightly higher than that of MnP (0.2−0.7 J kg^{-1} K^{-1}) [13] and $La_{0.67}Sr_{0.33}MnO_3$ [10] films (0.6−1.5 J kg^{-1} K^{-1}).

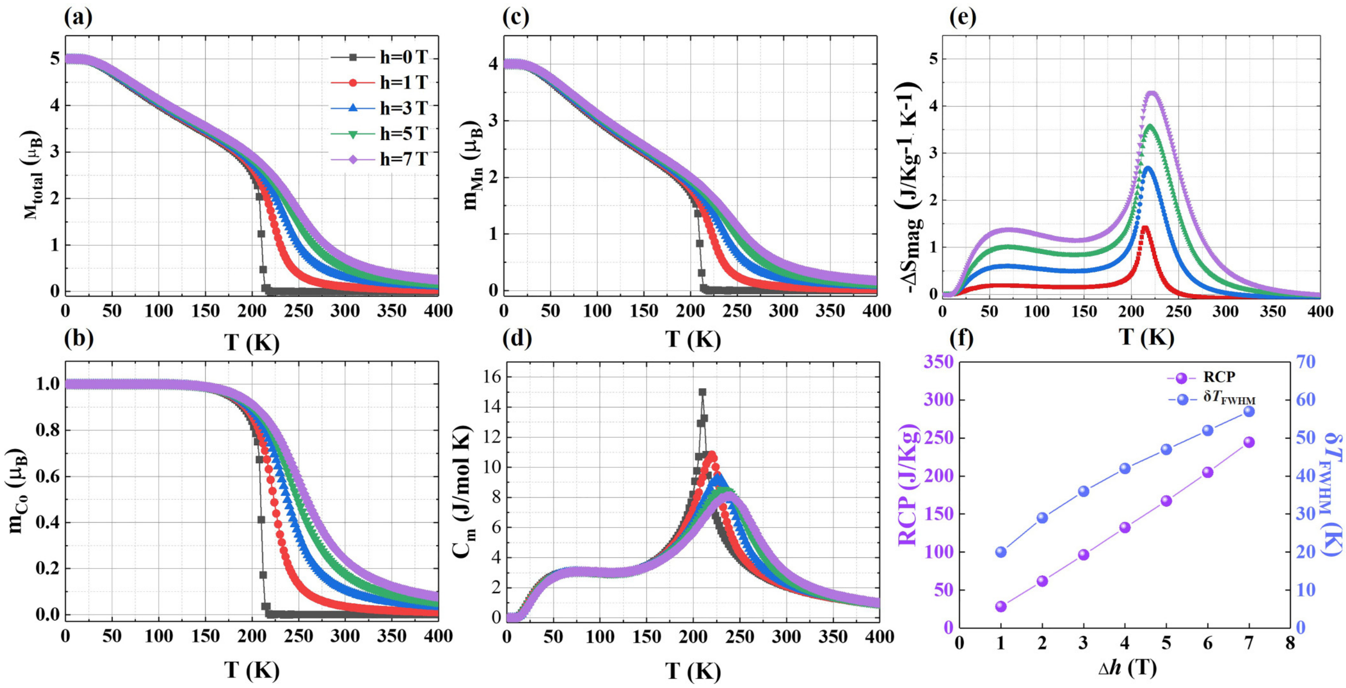

FIG. 3. Magnetization of (a) total, (b) Co, and (c) Mn atoms in 2D MnCoAs as a function of temperature from Monte Carlo simulations. (d) Specific heat C_m and (e) $-\Delta S_m$ for 2D MnCoAs. (f) RCP and δT_{FWHM} as a function of Δh for 2D MnCoAs.

Compared to conventional magnetocaloric films, 2D MnCoAs shows excellent MCE with a RCP value of $244.5\,\mathrm{J\,kg^{-1}}$ which is higher than $EuTiO_3$ ($152\,\mathrm{J\,kg^{-1}}$) [7], $EuO_{1-\delta}$ ($223\,\mathrm{J\,kg^{-1}}$) [14], $Gd_{100-x}Co_x$ ($106-158\,\mathrm{J\,kg^{-1}}$) [11], and $Gd_5Si_{1.3}Ge_{2.7}$ ($212\,\mathrm{J\,kg^{-1}}$) [16] films. Moreover, 2D MnCoAs has a much higher critical temperature (214–221 K) than Gd-based 2D MOF [19] and Cu-based inorganic-organic hybrids [17,18] ($T_N = 2$–34 K, $T_C = 12$ K).

To disclose the origin of abnormal bimodal behavior of specific heat and the pronounced MCE in 2D MnCoAs, the total energy is divided into four parts: $H = H^{(1)}_{\mathrm{Co-Co}} + H^{(2)}_{\mathrm{Co-Co}} + H_{\mathrm{Co-Mn}} + H_{\mathrm{Mn-Mn}}$:

$$H^{(1)}_{\mathrm{Co-Co}} = -J_1 \sum_{\langle i,j\rangle} S^A_i S^A_j - \frac{\mu_B g h}{2} \sum_i S^A_i, \tag{3}$$

TABLE I. The critical magnetic transition temperature T (K), magnetic entropy change ΔS_m ($\mathrm{J\,kg^{-1}\,K^{-1}}$), and RCP ($\mathrm{J\,kg^{-1}}$) values of common magnetocaloric films.

	T	ΔS_m	RCP	Reference
MnCoAs	214–223	1.4–4.9	28.4–324.7	Present work
$EuTiO_3$	3	24	152	[7]
$EuO_{1-\delta}$	142–144	6.4	223	[14]
MnP	275–300	0.2–0.7	13.1–29.5	[13]
$La_{0.67}Sr_{0.33}MnO_3$	312–321	0.6–1.5	34.2–50.2	[10]
FeRh	350	20	–	[9]
$Gd_{100-x}Co_x$	180–337	1.3–2.6	106–158	[11]
$Gd_5Si_{1.3}Ge_{2.7}$	192	8.8	212	[16]
$[(CH_2)_2(NH_3)_2]CuCl_4$	34	0.1	2	[17]
$(C_{12}H_{25}NH_3)_2CuCl_4$	13	1.9	4.2–18.2	[18]

$$H^{(2)}_{\mathrm{Co-Co}} = -J_3 \sum_{\langle m,n\rangle} S^A_m S^A_n - \frac{\mu_B g h}{2} \sum_i S^A_i, \tag{4}$$

$$H_{\mathrm{Co-Mn}} = -J_2 \sum_{\langle k,l\rangle} S^A_k S^B_l - \frac{D}{2} \sum_i \left(S^B_i\right)^2 - \frac{\mu_B g h \sum_i S^B_i}{2}, \tag{5}$$

$$H_{\mathrm{Mn-Mn}} = -J_3 \sum_{\langle m,n\rangle} S^B_m S^B_n - \frac{D}{2} \sum_i \left(S^B_i\right)^2 - \frac{\mu_B g h}{2} \sum_i S^B_i. \tag{6}$$

As shown in Fig. 4, the competition among different parts of energies induces a magnetic phase transition at T_C as well as a low-temperature anomaly. $H^{(1)}_{\mathrm{Co-Co}}$ and $H_{\mathrm{Co-Mn}}$ mainly contribute to the magnetic specific heat, suggesting that the magnetic behavior of 2D MnCoAs depends mainly on both Co-Co and Mn-Co interaction. As the magnetic field increases, the maximum of $\partial H^{(1)}_{\mathrm{Co-Co}}/\partial T$ shifts towards the high-temperature end, indicating that Co-Co interaction (J_1) provides a higher magnetic transition temperature than Mn-Co interaction. As discussed above, the ferromagnetic transition around T_C is a consequence of the magnetic behavior of completely ordered Co ions and partially polarized Mn ions. Because of $J_1 \gg J_2$ and the relatively large spin moment of the Mn ion, the magnetic moments of Co and Mn sublattices evolve at a different rate below T_C. When the Co ions form ferromagnetic ordering, they provide an internal field that enhances the polarization of the Mn ions through Mn-Co interaction. Simultaneously, the more polarized Mn ions make the ordered on-site moments of Co ions more robust against thermal perturbation through the Mn-Co interaction, resulting in a higher T_C of 214–221 K. Both $\partial H_{\mathrm{Co-Mn}}/\partial T$ and $\partial H_{\mathrm{Mn-Mn}}/\partial T$ exhibit an anomalous magnetic specific heat

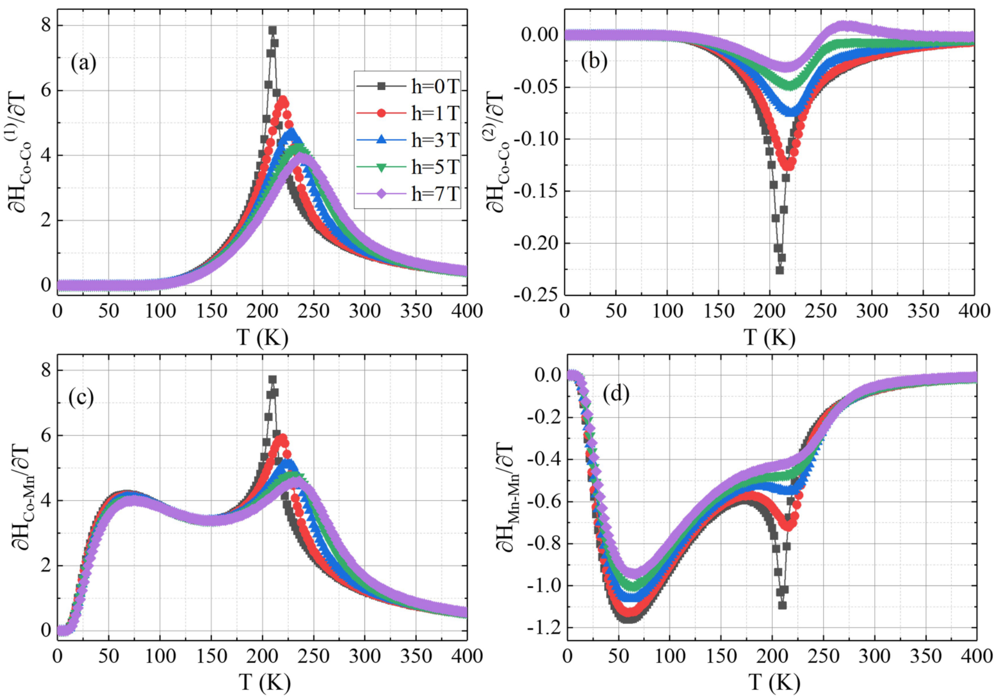

FIG. 4. The contribution to magnetic specific heat from Co-Co, Co-Mn, and Mn-Mn interactions. Calculated (a) $\frac{\partial H^{(1)}_{\mathrm{Co-Co}}}{\partial T}$, (b) $\frac{\partial H^{(2)}_{\mathrm{Co-Co}}}{\partial T}$, (c) $\frac{\partial H_{\mathrm{Co-Mn}}}{\partial T}$, and (d) $\frac{\partial H_{\mathrm{Mn-Mn}}}{\partial T}$ as a function of temperature.

at a temperature of $T_p = 60$ K, indicating that the bimodal behavior mainly originates from the Mn ions. Before the Mn ions become completely saturated at T_p, the continued polarization of Mn ions below T_C slowly reduces the magnetic specific heat. Because of the large spin moment of the Mn ions, the completely saturated Mn ions at T_p possess high thermal stability, meaning the anomaly at T_p is barely influenced by an external magnetic field.

As a matter of fact, the magnetocaloric effect reflects the interaction mechanism between magnetic ions. Specifically, Co-Co interaction provides a relatively high T_C, and the $2S + 1$ magnetic levels of Mn ions are all occupied at zero field due to its weak anisotropy. This produces high entropy and large magnetic moment, making 2D MnCoAs easily polarized by an external magnetic field. The Mn-Co interaction provides an external field to further polarize the Mn ions. Therefore, the MCE has a wide operation temperature span of 20 K ($\Delta h = 1$ T) to 57 K ($\Delta h = 7$ T), which benefits from the unique bimodal behavior of specific heat, higher ΔS_m ($1.4-4.3\,\mathrm{J\,kg^{-1}\,K^{-1}}$) and RCP ($28.4-244.5\,\mathrm{J\,kg^{-1}}$). All these features hold great promise for application as a refrigerant. Besides 2D MnCoAs, similar crystal structure and bonding properties are also obtained for 2D MnNiAs. As shown in Supplemental Material Fig. S9 [41], 2D MnNiAs is also a promising magnetocaloric material which has an even higher ΔS_m value ($4.7\,\mathrm{J\,kg^{-1}\,K^{-1}}$). This result further validates the universality of our proposed mechanism.

Next, it is highly desirable that 2D MnCoAs can be experimentally synthesized. To date, CVD is a standard technique to fabricate 2D crystals from nonlayered bulk materials. For example, 2D non-vdW crystals of CrTe, CrSe, Cr_2Te_3, FeTe, and Cr_5Te_8 were successfully prepared on Si/SiO_2 substrate using CVD [21,24,25,27,60]. Thus we speculated that a similar approach could be used to synthesize 2D MnCoAs. A $4\sqrt{2} \times 3\sqrt{2}$ supercell of a MnCoAs sheet was matched to a 3×4 supercell of a Si (001) substrate with a lattice mismatch of 1.2% and 1.4% for the a and b directions, respectively. As shown in Supplemental Material Fig. S10 [41], placing a 2D MnCoAs sheet on a Si (001) surface yields good lattice commensurability with minor structural distortion. The calculated binding energy for a MnCoAs sheet on a Si (001) substrate is -0.15 eV/atom, which is comparable to that of graphene on Cu (111) (-0.1 eV/atom) [61]. The small lattice mismatches and weak binding energy suggested the feasibility of experimental realization by epitaxial growth. Additionally, we examined the effect of the substrate on the magnetic behavior of 2D MnCoAs. On the Si substrate, the magnetic moment of the Mn atom remains $3.3\,\mu_B$, and the energy differences between FM and various AFM states still ensures the FM ground state of the supported MnCoAs (see Supplemental Material Table S4 [41]). As shown in Supplemental Material Fig. S11 [41], the Si substrates provide the injection of holes into the MnCoAs film, enhancing the itinerant magnetism that made its T_C value increase to 667 K [62]. However, the hole injection also decreases the Mn-Co interaction (0.11 meV), weakening the MCE, and the reduced ΔS_m is $0.4\,\mathrm{J\,kg^{-1}\,K^{-1}}$. As shown in Supplemental Material Fig. S12 [41], the operating temperature range of MnCoAs is broader than that of other magnetocaloric materials due to the bimodal behavior, which explains the higher RCP values of $153\,\mathrm{J\,kg^{-1}}$ in the MnCoAs/Si film. Therefore, the Si (001) substrate not only provides suitable support for depositing 2D MnCoAs compounds, but also provides an extra degree of freedom to tailor the magnetic properties.

Our findings for 2D MnCoAs should help improve the cycling stability required to obviate the mechanical brittleness inherent to typical magnetocaloric materials, e.g., $Gd_5Si_2Ge_2$, Heusler alloys, and La(Fe, $Si)_{13}$ [63]. To this end, we investigated the mechanical properties of 2D MnCoAs in terms of ideal strength and fracture toughness. The stress-strain response under biaxial tensile strains for 2D MnCoAs is plotted in Supplemental Material Fig. S13 [41]. The ideal strength is 10 GPa, and the critical breaking strain is about 30%. Such value is advantageous compared to other 2D magnets, such as CrI_3 and $CrCl_3$ whose highest sustained strains of 6.5% and 6.0% and ideal strength of 3.6 and 2.2 Gpa, respectively [64], indicate a highly ductile deformation behavior.

To obtain a more general overview of the dimensional effect on the magnetic behavior of the MnCoAs compound, we further study the MCE in bulk MnCoAs for comparison. In bulk MnCoAs, the evaluated T_C value is 245 K, which is slightly higher than 2D MnCoAs. The MAE value of bulk MnCoAs is increased to −0.4 meV per formula, which favors the in-plane anisotropy. (see Supplemental Material Table S5 [41]) The increased MAE value could counteract thermal fluctuations and reduce the MCE performance in bulk MnCoAs. Compared to 2D MnCoAs, there is an additional interlayer AFM Mn-Mn interaction (−1.03 meV) in bulk MnCoAs. The existence of interlayer Mn-Mn coupling not only enhanced the AFM coupling in bulk MnCoAs but also made the bimodal behavior disappear (see Supplemental Material Fig. S14 [41]). Moreover, the magnetic moment of the Mn ion (3.0 μ_B) is decreased. The increased MAE value, decreased magnetic moment, and disappearance of the bimodal behavior result in a very small MCE in bulk MnCoAs ($\Delta S_m = 0-0.2\,\mathrm{J\,kg^{-1}\,K^{-1}}$). Therefore, the reduced dimensionality of MnCoAs material could improve its MCE, which is different from previous reported magnetocaloric material such as $La_{0.7}Ca_{0.3}MnO_3$ films [12].

IV. CONCLUSION

In summary, we proposed 2D tetragonal non-vdW MnCoAs as a promising magnetocaloric material with high cycling stability. Due to direct Co-Co and Mn-Co exchange interactions, the predicted 2D MnCoAs exhibits robust ferromagnetism with Curie temperature up to 214 K and large magnetic moment of 3.3 μ_B/Mn atom, weak MAE of 0.17 meV/formula along the out of plane direction (which produces a high magnetic entropy change), and an anomalous bimodal specific heat curve. Under an external magnetic field, the Co-Co interaction provides high transition temperature, while the Mn-Co interaction further polarizes the Mn ions. Therefore, 2D MnCoAs possesses an excellent MCE with a high ΔS_m value of $1.4-4.3\,\mathrm{J\,kg^{-1}\,K^{-1}}$, a high RCP of $28.4-244.5\,\mathrm{J\,kg^{-1}}$, and a wide operation temperature range of 20–57 K. Encouragingly, 2D MnCoAs can be grown directly on a Si (001) substrate and it still retains the desired magnetic properties, endowing 2D MnCoAs as a promising candidate for on-chip cooling. To confirm the universality of this design strategy, another 2D non-vdW compound with same structure, i.e., MnNiAs, was also identified as a promising magnetocaloric material with large MCE ($\Delta S_m = 4.7\,\mathrm{J\,kg^{-1}\,K^{-1}}$). Moreover, compared to bulk MnCoAs, 2D MnCoAs exhibits a more distinct MCE, compared to other magnetocaloric materials. Our results not only highlight a unique way to design superior magnetocaloric materials near room temperature with large MCE, but also shed light on the mechanism of magnetovolume coupling at low-dimensional limits.

ACKNOWLEDGMENTS

This work was supported by the National Natural Science Foundation of China (Grants No. 12274050, No. 11874097, No. 91961204, and No. 11804044) and the Fundamental Research Funds for the Central Universities (Grants No. DUT22LAB104 and No. DUT22ZD103). The authors acknowledge the Supercomputing Center of Dalian University of Technology and Tianjin for providing the computing resources.

[1] V. Franco, J. S. Blázquez, J. J. Ipus, J. Y. Law, L. M. Moreno-Ramírez, and A. Conde, Magnetocaloric effect: From materials research to refrigeration devices, Prog. Mater. Sci. **93**, 112 (2018).

[2] N. R. Ram, M. Prakash, U. Naresh, N. S. Kumar, T. S. Sarmash, T. Subbarao, R. J. Kumar, G. R. Kumar, and K. C. B. Naidu, Review on magnetocaloric effect and materials, J. Supercond. Novel Magn. **31**, 1971 (2018).

[3] J. H. Belo, A. L. Pires, J. P. Araújo, and A. M. Pereira, Magnetocaloric materials: From micro- to nanoscale, J. Mater. Res. **34**, 134 (2018).

[4] X. Jiang, Q. Liu, J. Xing, N. Liu, Y. Guo, Z. Liu, and J. Zhao, Recent progress on 2D magnets: Fundamental mechanism, structural design and modification, Appl. Phys. Rev. **8**, 031305 (2021).

[5] S. B. Roy, First order magneto-structural phase transition and associated multi-functional properties in magnetic solids, J. Phys.: Condens. Matter **25**, 183201 (2013).

[6] S. Shaji, N. R. Mucha, P. Giri, C. Binek, and D. Kumar, Magnetic and magnetocaloric properties of Fe_2Ta thin films, AIP Adv. **10**, 025222 (2020).

[7] R. Das, R. Prabhu, N. Venkataramani, S. Prasad, L. Li, M.-H. Phan, V. Keppens, D. Mandrus, and H. Srikanth, Giant low-field magnetocaloric effect and refrigerant capacity in reduced dimensionality $EuTiO_3$ multiferroics, J. Alloys Compd. **850**, 156819 (2021).

[8] V. V. Khovaylo, V. V. Rodionova, S. N. Shevyrtalov, and V. Novosad, Magnetocaloric effect in "reduced" dimensions: Thin films, ribbons, and microwires of Heusler alloys and related compounds, Phys. Status Solidi B **251**, 2104 (2014).

[9] Y. Liu, L. C. Phillips, R. Mattana, M. Bibes, A. Barthelemy, and B. Dkhil, Large reversible caloric effect in FeRh thin films via a dual-stimulus multicaloric cycle, Nat. Commun. **7**, 11614 (2016).

[10] V. S. Kumar, R. Chukka, Z. Chen, P. Yang, and L. Chen, Strain dependent magnetocaloric effect in $La_{0.67}Sr_{0.33}MnO_3$ thin-films, AIP Adv. **3**, 052127 (2013).

[11] M. Tadout, C.-H. Lambert, M. El Hadri, A. Benyoussef, M. Hamedoun, M. Benaissa, O. Mounkachi, and S. Mangin, Magnetic properties and magnetocaloric effect in $Gd_{100-x}Co_x$ thin films, Crystals **9**, 278 (2019).

[12] P. Lampen, N. S. Bingham, M. H. Phan, H. Kim, M. Osofsky, A. Piqué, T. L. Phan, S. C. Yu, and H. Srikanth, Impact of reduced dimensionality on the magnetic and magnetocaloric response of $La_{0.7}Ca_{0.3}MnO_3$, Appl. Phys. Lett. **102**, 062414 (2013).

[13] C.-M. Hung, R. P. Madhogaria, B. Muchharla, E. M. Clements, A. T. Duong, R. Das, P. T. Huy, S. Cho, S. Witanachchi, H. Srikanth *et al.*, MnP films with desired magnetic, magnetocaloric, and thermoelectric properties for a perspective magneto-thermo-electric cooling device, Phys. Status Solidi A **219**, 2100367 (2021).

[14] P. Lampen-Kelley, R. Madhogaria, N. S. Bingham, M. H. Phan, P. M. S. Monteiro, N.-J. Steinke, A. Ionescu, C. H. W. Barnes, and H. Srikanth, Tablelike magnetocaloric effect and enhanced refrigerant capacity in $EuO_{1-\delta}$ thin films, Phys. Rev. Mater. **5**, 094404 (2021).

[15] N. Cortés, F. J. Peña, O. Negrete, and P. Vargas, Proximity-induced spin-polarized magnetocaloric effect in transition metal dichalcogenides, Phys. Rev. B **105**, 014443 (2022).

[16] R. L. Hadimani, J. H. B. Silva, A. M. Pereira, D. L. Schlagel, T. A. Lograsso, Y. Ren, X. Zhang, D. C. Jiles, and J. P. Araújo, $Gd_5(Si, Ge)_4$ thin film displaying large magnetocaloric and strain effects due to magnetostructural transition, Appl. Phys. Lett. **106**, 032402 (2015).

[17] S. Dutta, S. K. D. Vishnu, S. Som, R. Chaurasiya, D. K. Patel, K. Moovendaran, C.-C. Lin, C.-W. Chen, and R. Sankar, Segmented highly reversible thermochromic layered perovskite $[(CH_2)_2(NH_3)_2]CuCl_4$ crystal coupled with an inverse magnetocaloric effect, ACS Appl. Electron. Mater. **4**, 521 (2022).

[18] M. Bochalya and S. Kumar, Magnetocaloric effect in 2D-alkylammonium copper halides layered inorganic-organic systems, J. Appl. Phys. **127**, 055501 (2020).

[19] M. Orts-Arroyo, R. Rabelo, A. Carrasco-Berlanga, N. Moliner, J. Cano, M. Julve, F. Lloret, G. De Munno, R. Ruiz-Garcia, J. Mayans *et al.*, Field-induced slow magnetic relaxation and magnetocaloric effects in an oxalato-bridged gadolinium(III)-based 2D MOF, Dalton Trans. **50**, 3801 (2021).

[20] C. Jin and L. Kou, Two-dimensional non-van der Waals magnetic layers: Functional materials for potential device applications, J. Phys. D **54**, 413001 (2021).

[21] L. Meng, Z. Zhou, M. Xu, S. Yang, K. Si, L. Liu, X. Wang, H. Jiang, B. Li, P. Qin *et al.*, Anomalous thickness dependence of Curie temperature in air-stable two-dimensional ferromagnetic 1T-$CrTe_2$ grown by chemical vapor deposition, Nat. Commun. **12**, 809 (2021).

[22] H. Wu, W. Zhang, L. Yang, J. Wang, J. Li, L. Li, Y. Gao, L. Zhang, J. Du, H. Shu *et al.*, Strong intrinsic room-temperature ferromagnetism in freestanding non-van der Waals ultrathin 2D crystals, Nat. Commun. **12**, 5688 (2021).

[23] Z. Jin, Z. Ji, Y. Zhong, Y. Jin, X. Hu, X. Zhang, L. Zhu, X. Huang, T. Li, X. Cai *et al.*, Controlled synthesis of a two-dimensional non-van der Waals ferromagnet toward a magnetic moiré superlattice, ACS Nano **16**, 7572 (2022).

[24] Y. Wen, Z. Liu, Y. Zhang, C. Xia, B. Zhai, X. Zhang, G. Zhai, C. Shen, P. He, R. Cheng *et al.*, Tunable room-temperature ferromagnetism in two-dimensional Cr_2Te_3, Nano Lett. **20**, 3130 (2020).

[25] Y. Zhang, J. Chu, L. Yin, T. A. Shifa, Z. Cheng, R. Cheng, F. Wang, Y. Wen, X. Zhan, Z. Wang *et al.*, Ultrathin magnetic 2D single-crystal CrSe, Adv. Mater. **31**, 1900056 (2019).

[26] B. Tang, X. Wang, M. Han, X. Xu, Z. Zhang, C. Zhu, X. Cao, Y. Yang, Q. Fu, J. Yang *et al.*, Phase engineering of Cr_5Te_8 with colossal anomalous Hall effect, Nat. Electron. **5**, 224 (2022).

[27] L. Kang, C. Ye, X. Zhao, X. Zhou, J. Hu, Q. Li, D. Liu, C. M. Das, J. Yang, D. Hu *et al.*, Phase-controllable growth of ultrathin 2D magnetic FeTe crystals, Nat. Commun. **11**, 3729 (2020).

[28] J. Xu, W. Li, B. Zhang, L. Zha, W. Hao, S. Hu, J. Yang, S. Li, S. Gao, and Y. Hou, Free-standing 2D non-van der Waals antiferromagnetic hexagonal FeSe semiconductor: Halide-assisted chemical synthesis and Fe^{2+} related magnetic transitions, Chem. Sci. **13**, 203 (2022).

[29] L. Hu, L. Cao, L. Li, J. Duan, X. Liao, F. Long, J. Zhou, Y. Xiao, Y.-J. Zeng, and S. Zhou, Two-dimensional magneto-photoconductivity in non-van der Waals manganese selenide, Mater. Horiz. **8**, 1286 (2021).

[30] J. Peng, Y. Liu, H. Lv, Y. Li, Y. Lin, Y. Su, J. Wu, H. Liu, Y. Guo, Z. Zhuo *et al.*, Stoichiometric two-dimensional non-van der Waals $AgCrS_2$ with superionic behaviour at room temperature, Nat. Chem. **13**, 1235 (2021).

[31] Y. Gebredingle, M. Joe, and C. Lee, First-principles calculations of the spin-dependent electronic structure and strain tunability in 2D non-van der Waals chromium chalcogenides Cr_2X_3 ($X =$ S, Se, Te): Implications for spintronics applications, ACS Appl. Nano Mater. **5**, 10383 (2022).

[32] Y. Wei, C. Liu, H. S. Tsai, Y. Zhang, C. Qi, G. Ma, T. Wang, and M. Huo, Prediction of the abnormal properties in monolayer $\alpha-Al_xGa_{2-x}O_3$, Adv. Theory Simul. **3**, 2000102 (2020).

[33] J. Hafner, *Ab-initio* simulations of materials using VASP: Density-functional theory and beyond, J. Comput. Chem. **29**, 2044 (2008).

[34] G. Kresse and J. Furthmüller, Efficient iterative schemes for ab initio total-energy calculations using a plane-wave basis set, Phys. Rev. B **54**, 11169 (1996).

[35] P. E. Blöchl, Projector augmented-wave method, Phys. Rev. B **50**, 17953 (1994).

[36] J. P. Perdew, K. Burke, and M. Ernzerhof, Generalized Gradient Approximation Made Simple, Phys. Rev. Lett. **77**, 3865 (1996).

[37] A. Togo and I. Tanaka, First principles phonon calculations in materials science, Scr. Mater. **108**, 1 (2015).

[38] G. J. Martyna, M. L. Klein, and M. Tuckerman, Nosé–Hoover chains: The canonical ensemble via continuous dynamics, J. Chem. Phys. **97**, 2635 (1992).

[39] J. Xing, P. Wang, Z. Jiang, X. Jiang, Y. Wang, and J. Zhao, Rational design of 2D organic magnets with giant magnetic anisotropy based on two-coordinate 5*d* transition metals, APL Mater. **8**, 071105 (2020).

[40] J. Sivardière and M. Blume, Dipolar and quadrupolar ordering in $S = 3/2$ Ising systems, Phys. Rev. B **5**, 1126 (1972).

[41] See Supplemental Material at http://link.aps.org/supplemental/10.1103/PhysRevB.108.054427 for additional data, including the computational details and more simulation results of 2D MnCoAs. See also Refs. [42–46] therein.

[42] X. Xu, Y. W. Li, S. R. Duan, S. L. Zhang, Y. J. Chen, L. Kang, A. J. Liang, C. Chen, W. Xia, Y. Xu *et al.*, Signature for non-Stoner ferromagnetism in the van der Waals ferromagnet Fe_3GeTe_2, Phys. Rev. B **101**, 201104(R) (2020).

[43] Q. Liu, J. Xing, Z. Jiang, Y. Guo, X. Jiang, Y. Qi, and J. Zhao, Layer-dependent magnetic phase diagram in $Fe_nGeTe_2(3 \leqslant n \leqslant 7)$ ultrathin films, Commun. Phys. **5**, 140 (2022).

[44] J. Kanamori, Crystal distortion in magnetic compounds, J. Appl. Phys. **31**, S14 (1960).

[45] J. B. Goodenough, Theory of the role of covalence in the perovskite-type manganites [La, M(II)]MnO_3, Phys. Rev. **100**, 564 (1955).

[46] P. W. Anderson, New approach to the theory of superexchange interactions, Phys. Rev. **115**, 2 (1959).

[47] T. Krenke, E. Duman, M. Acet, E. F. Wassermann, X. Moya, L. Mañosa, and A. Planes, Inverse magnetocaloric effect in ferromagnetic Ni–Mn–Sn alloys, Nat. Mater. **4**, 450 (2005).

[48] R. Modak, R. Iguchi, H. Sepehri-Amin, A. Miura, and K.-i. Uchida, Simultaneous direct measurements of conventional and inverse magnetocaloric effects in Ni–Mn-based Heusler alloys using lock-in thermography technique, AIP Adv. **10**, 065005 (2020).

[49] D. H. Mosca, F. Vidal, and V. H. Etgens, Strain Engineering of the Magnetocaloric Effect in MnAs Epilayers, Phys. Rev. Lett. **101**, 125503 (2008).

[50] N. A. Zarkevich and V. I. Zverev, Viable materials with a giant magnetocaloric effect, cryst. **10**, 815 (2020).

[51] V. Johnson, Ternary transition metal germanides and arsenides, Mater. Res. Bull. **8**, 1067 (1973).

[52] M. Born and K. Huang, Dynamical theory of crystal lattices, Am. J. Phys. **23**, 474 (1955).

[53] C. M. Hurd, Varieties of magnetic order in solids, Contemp. Phys. **23**, 469 (1982).

[54] Y. Zhang and G. J. Miller, Competition between direct and indirect exchange couplings in MnFeAs: A first-principles investigation, J. Phys. Chem. C **119**, 580 (2014).

[55] M. H. Karigerasi, K. Kang, G. E. Granroth, A. Banerjee, A. Schleife, and D. P. Shoemaker, Strongly two-dimensional exchange interactions in the in-plane metallic antiferromagnet Fe_2As probed by inelastic neutron scattering, Phys. Rev. Mater. **4**, 114416 (2020).

[56] G. F. Newell and E. W. Montroll, On the theory of the Ising model of ferromagnetism, Rev. Mod. Phys. **25**, 353 (1953).

[57] J. W. Xu, X. Q. Zheng, S. X. Yang, L. Xi, D. S. Wang, C. F. Liu, J. Y. Zhang, Y. F. Wu, J. X. Shen, S. G. Wang *et al.*, Large reversible magnetic entropy change of $R_3Ni_6Al_2$(R = Dy, Ho and Er) compounds, J. Alloys Compd. **879**, 160468 (2021).

[58] Y. Liu, J. Li, J. Tao, Y. Zhu, and C. Petrovic, Anisotropic magnetocaloric effect in $Fe_{3-x}GeTe_2$, Sci. Rep. **9**, 13233 (2019).

[59] J. Yan, X. Luo, F. C. Chen, J. J. Gao, Z. Z. Jiang, G. C. Zhao, Y. Sun, H. Y. Lv, S. J. Tian, Q. W. Yin *et al.*, Anisotropic magnetic entropy change in the hard ferromagnetic semiconductor VI_3, Phys. Rev. B **100**, 094402 (2019).

[60] C. Chen, X. Chen, C. Wu, X. Wang, Y. Ping, X. Wei, X. Zhou, J. Lu, L. Zhu, J. Zhou *et al.*, Air-stable 2D Cr_5Te_8 nanosheets with thickness-tunable ferromagnetism, Adv. Mater. **34**, 2107512 (2022).

[61] D. Luo, X. You, B.-W. Li, X. Chen, H. J. Park, M. Jung, T. Y. Ko, K. Wong, M. Yousaf, X. Chen *et al.*, Role of graphene in water-assisted oxidation of copper in relation to dry transfer of graphene, Chem. Mater. **29**, 4546 (2017).

[62] M.-Y. Liu, Y. He, Y. Mao, and K. Xiong, High-temperature ferromagnetism and half-metallicity in hole-doped Janus OM_2S (M = Ga, In, and Tl) monolayers, Phys. Rev. B **105**, 035418 (2022).

[63] O. Glushko, A. Funk, V. Maier-Kiener, P. Kraker, M. Krautz, J. Eckert, and A. Waske, Mechanical properties of the magnetocaloric intermetallic $LaFe_{11.2}Si_{1.8}$ alloy at different length scales, Acta Mater. **165**, 40 (2019).

[64] F. Cantos-Prieto, A. Falin, M. Alliati, D. Qian, R. Zhang, T. Tao, M. R. Barnett, E. J. G. Santos, L. H. Li, and E. Navarro-Moratalla, Layer-dependent mechanical properties and enhanced plasticity in the van der Waals chromium trihalide magnets, Nano Lett. **21**, 3379 (2021).